J. Fluid Mech. (1993), *vol.* 257, *pp.* 311–337

Vortex ring pairs: numerical simulation and experiment

By P. D. WEIDMAN[1] AND N. RILEY[2]

[1] Department of Mechanical Engineering, University of Colorado, Boulder, CO 80309, USA

[2] School of Mathematics, University of East Anglia, Norwich, NR4 7TJ, UK

In this paper we discuss the possibility that concentric vortex rings, with associated circulation of opposite sign, can propagate steadily as a coherent pair. Inviscid flow considerations suggest that such a configuration, which we define as a vortex ring pair, may be possible. Numerical solutions of the Navier–Stokes equations for incompressible, laminar flow show that, although diffusion results in a continual redistribution of vorticity, a quasi-steadily propagating vortex ring pair could be attained in practice. Experiments are reported to test this idea by generating counter-rotating vortex ring pairs by impulsive fluid motion through an annular orifice. Depending on the normalized impulse and the orifice radius ratio, the vortex rings are observed either (i) to propagate together until diffusive effects or vortex ring instability destroys the coherent motion, or (ii) the inner ring propagates to some maximum axial distance where it reverses its direction and returns to the orifice wall, leaving the outer ring free to continue its forward motion unabated. Numerical simulation shows that the stable flow of the vortex ring trajectories can be reasonably well reproduced. The boundary separating motion (i) from (ii) and the normalized inner ring penetration distance are found over the range of impulse and radius ratio covered by the experiments. Other observed features of vortex ring motion including self-similar trajectories of the spiral core centres during vortex sheet roll-up and ring instability are also presented.

1. Introduction

The dynamics of vortex rings have long held a fascination for fluid dynamicists, as the recent authoritative review article by Shariff & Leonard (1992) demonstrates, and indeed were of great concern to those nineteenth century giants, Kelvin and Helmholtz. An interesting historical perspective of their work is given by Acheson (1990). Both Kelvin and Helmholtz illustrated the fact that two like vortex rings, in tandem with a common axis of symmetry, will tend to proceed in a leapfrogging manner through one another. A modern illustration of this is provided by Yamada & Matsui (1978); see also Van Dyke (1982). This leapfrogging motion is readily explained qualitatively in terms of the self-induced motion of each ring, and the mutual interaction between them. Both effects result in a propulsive motion of the rings in the same axial direction, whilst the second effect also accounts for variations in the ring radii. The fluid motion is a highly unsteady one.

In the present paper we also investigate the axisymmetric flow properties of interacting vortex rings. However, unlike the situation described above, we assumed that the circulation associated with each of our rings differs in sign. The particular question we address is whether or not two such rings, with different radii and placed concentrically, can result in a steady flow in the form of a propagating vortex ring pair.

Qualitative arguments suggest that this might be possible as follows. The mutual interaction between the rings acts to push them in the same direction, which is the direction in which the outer ring would be self-propelled in the absence of the inner. By contrast the self-induced velocity of the inner ring is in the opposite direction; indeed, if it were sufficiently strong one might suppose that it would separate from the outer ring and propagate in the opposite direction. On the other hand, if the inner ring's self-induced velocity were sufficiently weak then it would be pushed through and ahead of the outer ring by their mutual interaction. This in turn suggests that a delicate balance may exist between the two rings such that they propagate together as a coherent vortex ring pair. It can be readily be shown for an inviscid fluid, if we make the approximations that the rings are thin and the vorticity within them is uniform, that the concept of a vortex ring pair propagating steadily is a valid one. That such a steady, or even quasi-steady, flow is possible in a viscous fluid is not at all obvious owing to the continuous redistribution of vorticity by diffusion. In this paper we investigate such a possibility by numerical simulation and laboratory experimentation.

We note that coaxial counter-rotating vortex rings appear naturally in rather different fluid dynamic situations. The formation of a secondary counter-rotating vortex ring is often observed during the head-on collision of a primary vortex ring with a plane wall or a free liquid surface (Magarvey & MacLatchey 1964; Yamada & Matsui 1982; Cerra & Smith 1983) and has recently attracted much attention from the computational fluid dynamics community (Orlandi 1990; Dommermuth & Yue 1990; Swearingen, Crouch & Handler 1993). In this event a shear region of sign opposite that of the incident ring develops between the ring and the wall, and the vortical fluid rolls up to form a secondary vortex ring. This weaker vortex ring is then induced to propagate around and inside the primary ring, where circumferential corrugations develop, each of which grow in amplitude and wraps in tongue-like fashion around the primary vortex ring. Lasheras, Lecuona & Rodriguez (1991) report similar features in the moving frame of a co-flowing jet. With large-amplitude axial forcing, a ring structure composed of an array of counter-rotating vortex-ring pairs with the outer, weaker ring surrounding the inner primary ring has been observed. Amplification of an azimuthal instability on the inner ring deforms the outer ring to such an extent that circumferential corrugations on the latter pinch off and reconnect to form an array of vortex loops spaced uniformly around the inner ring. These complicated, but interesting, induced vortex motions occur only when the counter-rotating vortex rings stay in close proximity over a sufficient length of time. In the former situation the wall traps the rings while in the latter event coherence of the ring pairs is a direct result of the periodic axial forcing. The primary structure in each case is the vortex ring pair, and the experiments described above show that such a ring pair can be highly unstable.

Nevertheless, numerical simulations presented here at sufficiently low Reynolds number show that a balance may be struck between ring–ring induced motions and vortex diffusion such that the ring pair persists without instability for an appreciable period of time. In the present experiments, an apparatus has been designed to generate laminar counter-rotating vortex rings by impulsive motion of liquid (water) through an annular orifice. Kambe & Takao (1971), in an investigation of the motion of distorted vortex rings, reported a single experiment of this type in air using an annular orifice which we interpret (see the Appendix) to have an orifice radius of 0.6. After formation of the coaxial rings by impulsive piston displacement, they observed the immediate return of the inner ring and its collision with the orifice wall.

Our paper is organized as follows. In §2 we describe the numerical approach we have adopted for the laminar axisymmetric flows under consideration. This consists of a

standard alternating-direction implicit method employed in a time-marching solution of the unsteady Navier–Stokes equations. These numerical results are discussed in §3; principal amongst these is the discovery that quasi-steadily propagating vortex ring pairs are a viable proposition, before diffusion brings about their ultimate decay. Details of the experimental facility capable of producing counter-rotating vortex rings over a range of piston-generated impulse motions through five separate annular orifices are given in §4. Also described in §4 are the measurement techniques used to determine fluid impulse, piston program factor, and vortex ring trajectories. Features of ring pair formation, flow asymmetries, ring instabilities and inner ring penetration distance are presented in §5 and, when possible, compared with analogous results for single vortex rings generated through circular tubes. Comparisons of the viscous numerical simulations with measured trajectories are presented in §6. A discussion of results and concluding remarks are given in §7.

2. Governing equations and solution method

Helmholtz's equation for the vorticity $\boldsymbol{\omega}'$ may be written as

$$\frac{\partial \boldsymbol{\omega}'}{\partial t'} - \boldsymbol{\nabla} \times (\boldsymbol{v}' \times \boldsymbol{\omega}') = \nu \nabla^2 \boldsymbol{\omega}', \tag{2.1}$$

where ν is the kinematic viscosity, $\boldsymbol{v}'$ is the velocity, t' time and

$$\boldsymbol{\omega}' = \boldsymbol{\nabla} \times \boldsymbol{v}', \quad \boldsymbol{\nabla} \cdot \boldsymbol{v}' = 0. \tag{2.2a, b}$$

We are concerned with the dynamics of pairs of axisymmetric vortex rings in a circular cylindrical container of radius a and length l. We work with cylindrical polar coordinates (r', θ, z'), such that the containing cylinder is defined by $r' = a, z' = 0, l$; the corresponding velocity components are (u', v', w'). If γ_0 is the initial circulation about the outer vortex ring of the pair, then physical variables are made dimensionless with the length a, time a^2/γ_0, velocity γ_0/a and vorticity γ_0/a^2. We assume both that the flow is axisymmetric and that there is no azimuthal flow, so that $\boldsymbol{v} = (u, 0, w)$ and $\boldsymbol{\omega} = (0, \zeta, 0)$ where $\zeta = \partial u/\partial z - \partial w/\partial r$. Equation (2.2$b$) is satisfied by the introduction of a stream function ψ such that

$$u = \frac{1}{r}\frac{\partial \psi}{\partial z}, \quad w = -\frac{1}{r}\frac{\partial \psi}{\partial r}. \tag{2.3}$$

We choose to work not with the vorticity component ζ but with a vorticity function defined as

$$\Gamma = -r\zeta = r\left(\frac{\partial w}{\partial r} - \frac{\partial u}{\partial z}\right). \tag{2.4}$$

The θ-components of each of (2.1), (2.2a) then give, respectively,

$$\frac{\partial \Gamma}{\partial t} + u\frac{\partial \Gamma}{\partial r} + w\frac{\partial \Gamma}{\partial z} - \frac{2u\Gamma}{r} = \frac{1}{Re}\mathrm{D}^2\Gamma, \tag{2.5a}$$

$$\mathrm{D}^2\psi = -\Gamma, \tag{2.5b}$$

where $\mathrm{D}^2 = \partial^2/\partial r^2 - r^{-1}\partial/\partial r + \partial^2/\partial z^2$, and $Re = \gamma_0/\nu$ is the Reynolds number. Our

computational domain is defined as $0 \leqslant r \leqslant 1, 0 \leqslant z \leqslant z_0$, where $z_0 = l/a$, for which we require boundary conditions as follows:

$$\psi = u = \frac{\partial w}{\partial r} = \Gamma = 0, \quad r = 0, \quad 0 \leqslant z \leqslant z_0, \tag{2.6a}$$

$$\psi = u = w = 0; \quad \Gamma = \frac{\partial w}{\partial r}, \quad r = 1, \quad 0 \leqslant z \leqslant z_0, \tag{2.6b}$$

$$\psi = u = w = 0; \quad \Gamma = -r\frac{\partial u}{\partial z}, \quad 0 \leqslant r \leqslant 1, \quad z = 0, z_0. \tag{2.6c}$$

The conditions (2.6) hold for all time t. For an initial distribution of vorticity, at $t = t_0$ say, we approximate the vorticity associated with each ring by a viscous line vortex (Lamb 1932), which will be justified when the dimensions of the cross-section of a ring are small compared with its radius of curvature. Thus, with the outer and inner rings located at (r_o, z_o), (r_i, z_i) respectively, at initial time $t = t_0$ we have

$$\frac{\Gamma}{r} = -\frac{Re}{4\pi t_0}\left[\exp\{-Re[(r-r_o)^2+(z-z_o)^2]/4t_0\}+\frac{\gamma_i}{\gamma_o}\exp\{-\mathrm{Re}[(r-r_i)^2+(z-z_i)^2]/4t_0\}\right], \tag{2.7}$$

where γ_i is the initial circulation about the inner ring.

Equations (2.5), together with boundary conditions (2.6) and initial condition (2.7), are solved using finite-difference methods. We work with a uniform grid in the (r, z)-plane of dimensions $m \times n$, so that the grid spacings δr, δz are defined as $\delta r = (m-1)^{-1}$, $\delta z = z_0(n-1)^{-1}$, and the values of ψ and Γ at each grid point, namely $\psi_{i,j}$ and $\Gamma_{i,j}$, $1 \leqslant i \leqslant m$, $1 \leqslant j \leqslant n$, are determined for each $t > t_0$. Since (2.5a) is parabolic we can march the vorticity function forward in t, with steps of size δt, whilst ensuring that the elliptic equation (2.5b) and the boundary conditions (2.6) are satisfied throughout. To initiate the calculation initial conditions at $t = t_0$ are required on this mesh. Values of $\Gamma_{i,j}$ are provided by (2.7), from which we may deduce values of $\psi_{i,j}$ by direct integration of (2.5b) in the manner indicated below.

In both of equations (2.5) all spatial derivatives are represented, in the finite-difference formulation, by central differences. And with values for $\Gamma_{i,j}$ given, the discretized equation (2.5b) is solved iteratively by line relaxation. We solve the finite-difference approximation to (2.5a) using an alternating-direction implicit (ADI) method. Let the solution for $\Gamma_{i,j}$ at time t be $\Gamma^k_{i,j}$; we then wish to obtain the solution at the interior grid points at time $t+\delta t$, namely $\Gamma^{k+1}_{i,j}, 2 \leqslant i \leqslant m-1, 2 \leqslant j \leqslant n-1$. We assume, at this juncture, that ψ and all boundary values are known at both t and $t+\delta t$. The ADI method then involves splitting the time step into two equal half-steps and advancing the vorticity function over each half-step in turn, so that an intermediate solution, $\Gamma^{k+\frac{1}{2}}_{i,j}$, at $t+\frac{1}{2}\delta t$ is obtained. Over the first half-step, from t to $t+\frac{1}{2}\delta t$, r-derivatives of Γ are evaluated at time $t+\frac{1}{2}\delta t$, using central differences, whilst z-derivatives are evaluated at time t. This results in a tridiagonal system of algebraic equations, which are solved in the usual way by forward and back substitution, from which $\Gamma^{k+\frac{1}{2}}_{i,j}$ is determined. Over the second half-step, from $t+\frac{1}{2}\delta t$ to $t+\delta t$, r-derivatives of Γ are evaluated at time $t+\frac{1}{2}\delta t$, with z-derivatives evaluated at time $t+\delta t$. A tridiagonal system again results, from which $\Gamma^{k+1}_{i,j}$ is determined. Throughout the two half-time steps described above all other quantities are evaluated at $t+\frac{1}{2}\delta t$. When advancing (2.5a) one time step from time t we assume that $\psi^{k+1}_{i,j}$ and, when the no-slip boundary condition is enforced, the boundary values $\Gamma^{k+1}_{i,j}$, $2 \leqslant j \leqslant n-1$, $\Gamma^{k+1}_{i,l}$, $\Gamma^{k+1}_{i,n}$, $2 \leqslant i \leqslant m-1$ are known at time $t+\delta t$. Since this is not immediately true the following

procedure is pursued. First, estimates of these quantities are made by extrapolating from the two previous time steps. Using these estimates and the complete solution at time t, namely $\psi^k_{i,j}$, $\Gamma^k_{i,j}$, (2.5a) is solved as described above to obtain a first estimate of $\Gamma^{k+1}_{i,j}$. Solution of (2.5b) and evaluation of the wall vorticity, in the manner described below, gives revised estimates of $\psi^{k+1}_{i,j}$, $\Gamma^{k+1}_{m,j}$, $\Gamma^{k+1}_{i,l}$, and $\Gamma^{k+1}_{i,n}$. These new values can then be used to advance, again, the solution for Γ from time t and a better estimate of $\psi^{k+1}_{i,j}$, $\Gamma^{k+1}_{i,j}$ is thus obtained. This iteration within a time step continues until successive iterates differ by an amount which is less than a tolerance set for the calculation. To complete this discussion of our numerical procedures, the vorticity function at the solid boundaries must be calculated to ensure that the no-slip condition is satisfied there. Following Woods' (1954) method we have

$$(2-\delta r)\,\Gamma_{m,j} = -\Gamma_{m-1,j} - 6\frac{\psi_{m-1,i}}{\delta r^2}, \quad 2 \leqslant j \leqslant n-1,$$

$$\Gamma_{i,1} = -\tfrac{1}{2}\Gamma_{i,2} - 3\frac{\psi_{i,2}}{\delta z^2}, \quad 2 \leqslant i \leqslant m-1,$$

$$\Gamma_{i,n} = -\tfrac{1}{2}\Gamma_{i,n-1} - 3\frac{\psi_{i,n-1}}{\delta z^2}, \quad 2 \leqslant i \leqslant m-1.$$

The procedures we have outlined above ensure the formal accuracy of our solution to $O(\delta r^2, \delta z^2, \delta t^2)$.

We describe in §3 results obtained by the method set out above. In all the examples considered we choose $Re = 2000$, a value typical of our experiments as described in §5, and take $t_0 = 0.05$. The initial values r_o and r_i also encompass the range of our experimental values. For all results presented here we have set $\delta r = \delta z = 0.005$ and $\delta t = 0.001$. Numerical experimentation shows these values to be adequate for our purposes.

3. Numerical results

One of the aims of the present investigation is to examine the validity of the concept of a vortex ring pair. This we have defined, in §1, as a pair of concentric vortex rings, with associated circulation of opposite sign, which propagate as a coherent unit. Evidence in favour of the concept is provided by a simple calculation based upon an inviscid model with thin vortex rings that have cores of uniform vorticity. Figure 1 depicts two vortex rings having equal circular cross-sections of radius $\bar{a}$, with outer and inner radii of the rings, measured to the section centre, r_o and r_i respectively, a notation consistent with that in (2.7). For this situation Weidman (unpublished) has shown that a vortex ring pair is established for

$$\frac{\gamma_i}{\gamma_o} = \frac{\left(\dfrac{E_1(k)}{1-\delta} + \dfrac{F_1(k)}{1+\delta}\right) - \dfrac{1}{2}\left(\ln\left(\dfrac{8r_o}{\bar{a}}\right) - \tfrac{1}{4}\right)}{\left(\dfrac{E_1(k)}{1-\delta} - \dfrac{F_1(k)}{1+\delta}\right) + \dfrac{1}{2\delta}\left(\ln\left(\dfrac{8r_o}{\bar{a}}\right) + \ln\delta - \tfrac{1}{4}\right)}, \tag{3.1}$$

where γ_o, γ_i again represent the circulation about each of the outer and inner rings, respectively, $\delta = r_i/r_o$ is the radius ratio of the ring system, and the modulus of the complete elliptic integrals $F_1(k)$ and $E_1(k)$ is $k = 2\delta^{\frac{1}{2}}/(1+\delta)$. The result (3.1) assumes that the spacing of the rings is small compared with their mean radius, and that the core dimensions are small compared with the spacing. For a viscous fluid the situation is not

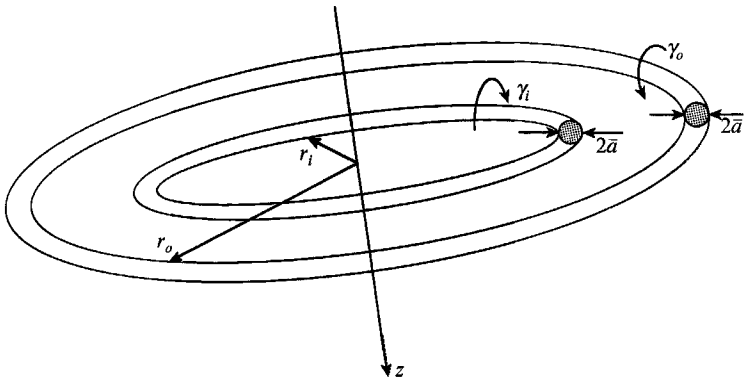

FIGURE 1. Schematic diagram of a vortex ring pair with equal core radii $\bar{a}$.

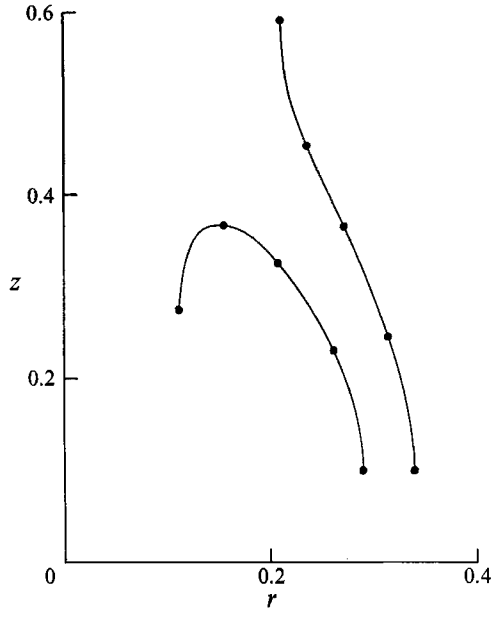

FIGURE 2. Vortex core trajectories: $r_o = 0.34$, $r_i = 0.29$ ($\Delta = 0.05$, $\delta = 0.853$), $\gamma_i/\gamma_o = -0.97$, $Re = 2000$. The markers indicate the core positions at successive times 0.05, 0.1, 0.15, 0.2, 0.3.

so clear cut. Diffusion results in a continuous redistribution of vorticity and ultimately, of course, the vortex rings will decay. At best, therefore, only a quasi-steady situation can be envisaged. The experiments described in §5 often result in a separation of the two vortex rings, and in our simulations we consider such situations also.

We begin by showing, in figure 2, a situation that is quite typical of the observations we have made in our experiments. In this diagram the trajectories of the cores of the vortex rings at a particular azimuthal section are plotted. The core has been defined to be the point within the cross-section of each vortex ring at which the vorticity takes its extreme value. This is located for each ring by interpolation. To interpret figure 2 we must relate it to the two competing influences under which the vortex rings move. There is, first, the mutual interaction between the two rings. As for a rectilinear vortex pair there is a tendency for each to convect the other along, instantaneously in a direction perpendicular to the line joining them. In addition, a curved vortex will

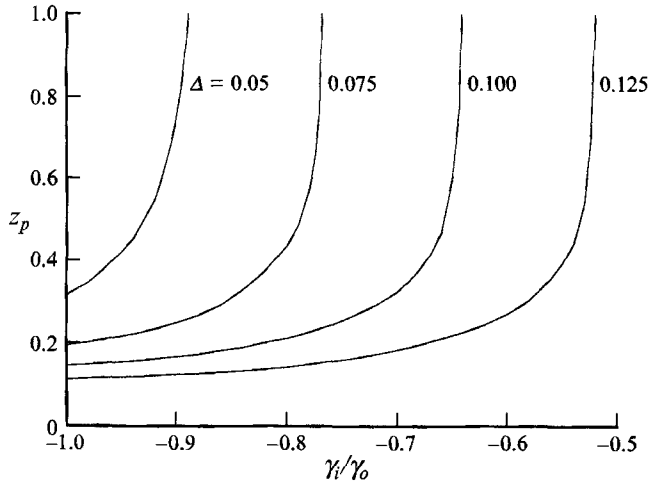

FIGURE 3. The penetration depth z_p of the inner vortex core as a function of the circulation ratio γ_i/γ_o for various values of $\Delta = r_o - r_i = r_o(1-\delta)$. $Re = 2000$, $r_o = 0.34$.

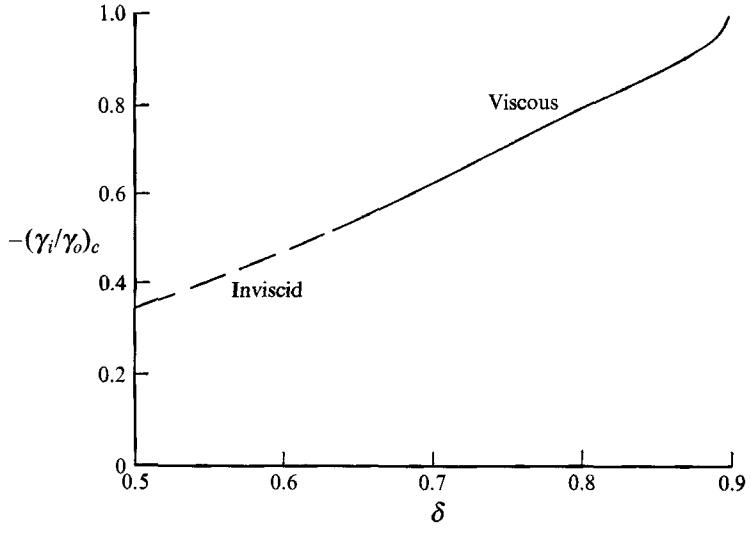

FIGURE 4. The critical value $(\gamma_i/\gamma_o)_c$ that yields a vortex ring pair, as a function of $\delta = r_i/r_o$. The full line corresponds to the viscous calculations with $Re = 2000$, $r_o = 0.34$; the broken line is the result (3.1) with $r_o = 0.34$, $\bar{a} = 0.02$.

induce a velocity upon itself. For our vortex rings this second influence, given that they have vorticity of opposite sign, tends to pull them apart. It is only a subtle balance between these two effects that can result in the establishment of a vortex ring pair. That balance is reflected in (3.1) for thin inviscid vortex rings. For the case shown in figure 2 separation takes place at $t \approx 0.2$. Up to that time the rings have been steadily diminishing in radius. This is a consequence of the mutual interaction between them, for as soon as the inner ring slips behind the outer, owing to the self-induced velocity effect, the velocity at each core has a radially inward component. Once separation of the rings has occurred the mutual interaction effect becomes negligible and the two rings propagate in opposite directions, each largely uninfluenced by the presence of the other.

The distance to which the inner ring will penetrate, z_p say, before separation takes place, will clearly depend upon the two parameters γ_i/γ_o and $\delta = r_i/r_o$, or $\Delta = r_i - r_o$. In figure 3 we show, for various values of Δ, the penetration depth z_p as a function of γ_i/γ_o. The critical value $(\gamma_i/\gamma_o)_c$ for which a vortex ring pair, as we have conceived it, is established is not difficult to identify even though our computational domain extends only to $z = z_0 = 1$, close to which we can expect wall interference effects. We believe, and we discuss a particular example below, that it is possible to recognize such a pair, even in what is at best a quasi-steady situation for a viscous fluid. The values of γ_i/γ_o so determined provided the results for $z = z_p = 1$ in figure 3. The very steep slopes of the curves depicted in figure 3 as $z_p \to 1$ help to confirm the values of $(\gamma_i/\gamma_o)_c$ in the sense that for $z_p \geqslant 0.9$, approximately, only very small changes in γ_i/γ_o are required to bring about enormous changes in z_p. We see clearly from figure 3 that as Δ, the initial distance between the rings, increases then a given penetration depth is achieved by reducing the value of $-\gamma_i/\gamma_o$, as might be expected. Conversely, if we fix γ_i/γ_o, then as the initial distance between the two rings increases the penetration depth decreases. Again this is a forseeable trend, since as that distance increases the self-induced motion of each ring becomes increasingly dominant when compared with the mutual interaction between them.

In figure 4 we show the values of $(\gamma_i/\gamma_o)_c$ as a function of δ. Also included is the result (3.1) for inviscid vortex ring pairs, within its range of validity, for which we have chosen the remaining parameter $\bar{a} = 0.020$. We recall that our viscous calculations are for a Reynolds number $Re = 2000$. On account of the limitations of the available computing resources it has not been possible to provide results for $(\gamma_i/\gamma_o)_c$, as shown in figure 4, for a range of values of Re. However, sample calculations show that for a given value of $(\gamma_i/\gamma_o)_c$ the effect of increasing Re is to increase δ, that is to decrease the initial distance Δ between the rings. In the experiments to be described δ may be fixed. Although a degree of control could be exercised over Re, even though it was not possible to predetermine this, no control could be exercised over γ_i/γ_o. In many cases $|\gamma_i/\gamma_o|$ proved to be too large, and a separation of the rings, of the type shown in figure 2, took place. Nevertheless, situations have been observed which correspond to the formation of a vortex ring pair, although rapid diffusion of vorticity and/or ring instability does quickly lead to the mutual destruction of the constituent vortex rings.

Finally, in figure 5 we demonstrate the features, noted in our simulation, associated with an example of a vortex ring pair. In figure 5(*a*) we show the trajectories of the vortex cores and, even though we have a quasi-steady rather than steady flow, we see that the integrity of the configuration is sensibly maintained until the endwall is approached. Although interaction of the vortex rings with the endwall is not our major concern in this paper, we do note some interesting features of it. As the wall is approached its effect is to decrease the radius of the inner ring and increase that of the outer. The mutual interaction between the rings then rapidly diminishes and the inner ring, with its self-induced velocity, moves back in its preferred direction. The outer ring, meanwhile, drives on causing a separation of the flow from the endwall. This manifests itself, as shown, as a 'bouncing' of the ring from the wall. In this process, which *inter alia* we have observed in our experiments, vorticity of opposite sign is swept from the wall around and into the vortex ring, with diffusion acting to rapidly destroy it. In figure 5(*b*) we show the time-variation of features of the outer of the two rings in the vortex ring pair. This diagram emphasizes the quasi-steadiness of the situation. Although there is only a relatively slow variation in radius of both the vortex core and its axial velocity, we see that diffusion acts to reduce rapidly the magnitude of the vorticity at the core. Figure 5(*c*) compares these quantities with the corresponding

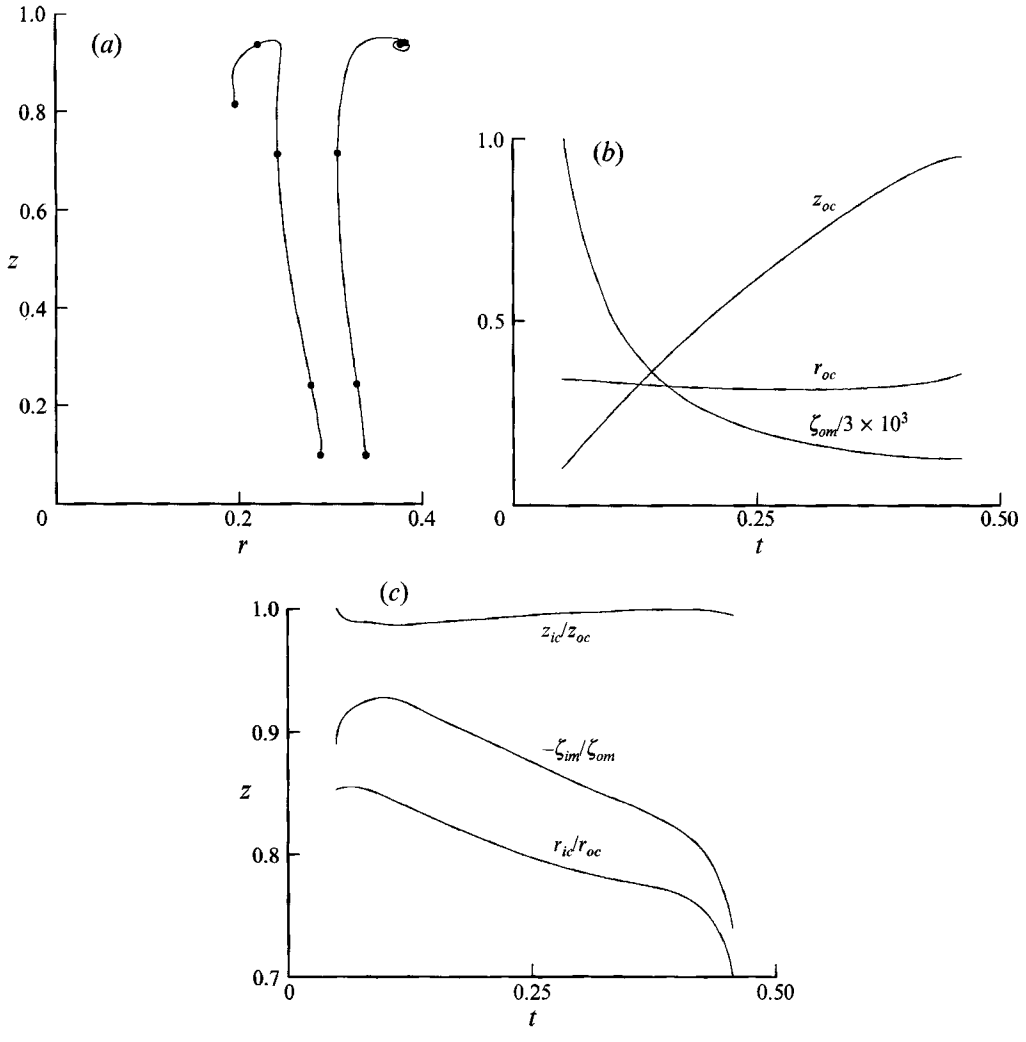

FIGURE 5. (*a*) Vortex core trajectories: $r_o = 0.34$, $r_i = 0.29$ ($\Delta = 0.05$, $\delta = 0.853$), $\gamma_i/\gamma_o = -0.89$, $Re = 2000$. The markers indicate the core positions at the successive non dimensional times 0.05, 0.1, 0.3, 0.5, 0.7. (*b*) The variation with time of the outer vortex core position (r_{oc}, z_{oc}), and the vorticity ζ_{om} associated with it, for the example of (*a*). (*c*) A comparison, as a function of time, of the outer (r_{oc}, z_{oc}) and inner (r_{ic}, z_{ic}) vortex core positions, and the associated vorticity extrema ζ_{im}, ζ_{om} for the example of (*a*).

quantities associated with the inner ring. Again, the quasi-steady nature of the flow is emphasized. Notice, in particular, the very small variation, 1.3% over the time span of the calculation, in the axial position z_{ic}/z_{oc} of the constituent ring cores; this, along with the results in figure 5(*a*), clearly exhibits the persistence of the vortex ring pair configuration.

4. Experimental apparatus and measurement procedure

A schematic of the experimental apparatus constructed from Plexiglas is given in figure 6(*a*), with a detailed drawing of the vortex ring pair generator in figure 6(*b*). The impulsive motion of liquid through the annular orifice O is provided by the motion of

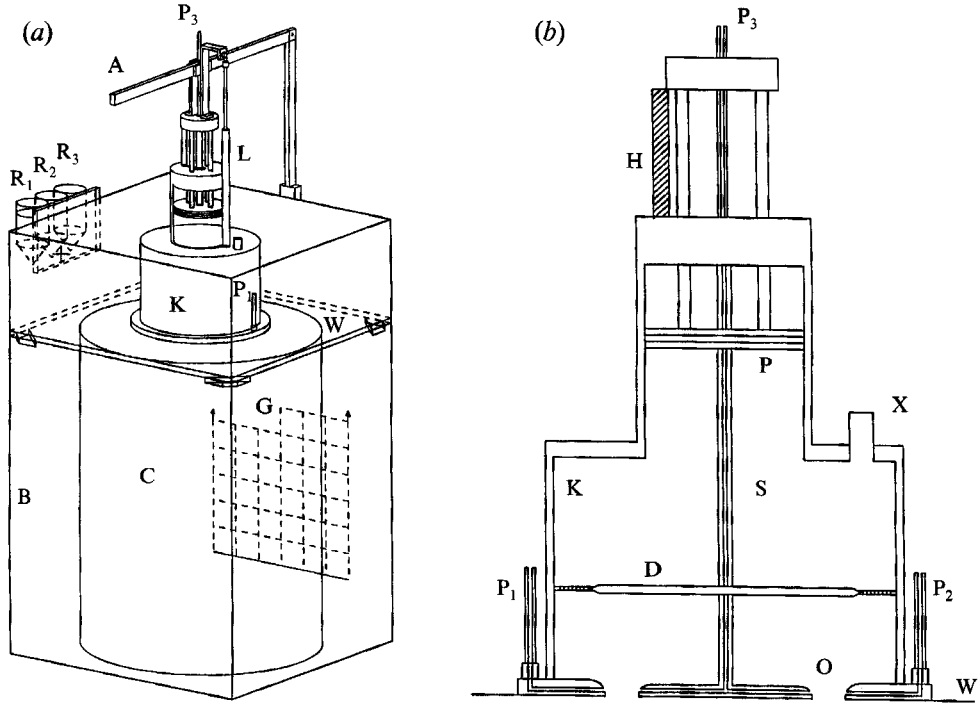

FIGURE 6. Schematic diagrams of (*a*) the experimental apparatus and (*b*) the vortex ring pair generator. See text for discussion of component parts.

Disk	d_i (cm)	W (cm)	A (cm^2)	$\bar{U}_0/\bar{U}_p$	δ
1	11.44	3.89	187.23	0.647	0.595
2	13.95	2.63	137.14	0.884	0.726
3	15.37	1.92	104.45	1.160	0.800
4	16.00	1.61	88.98	1.362	0.833
5	16.66	1.28	72.05	1.682	0.876

TABLE 1. Annular orifice geometry showing inner disk diameter d_i, gap width $\frac{1}{2}W = r_o - r_i$, orifice area A and radius ratio δ, and the velocity ratio between piston speed $\bar{U}_p$ and orifice fluid velocity $\bar{U}_0$

piston P manually actuated by depression of overhead link arm A. The piston chamber opens to cavity K which sits on top of wall W, horizontally fixed to four gussets in the corners of surrounding box B. The plate forming the outer orifice boundary of diameter d_o is mounted flush with the horizontal wall, and interchangeable circular plates attached to central shaft S have inner orifice diameters d_i. Open cylinder C of diameter $2a = 57.5$ cm projecting 76.2 cm downward inside box B provides the axisymmetric test region boundary and is attached by a ring of bolts to W. The 2 cm gap at tank bottom between C and B allows for movement of water displaced downward by the piston back up between the sidewalls of C and B through vents in W to raise slightly the free surface level. Dimensions, areas and other relevant features of the annular orifice and piston chamber are given in table 1.

The time history of piston movement is measured by a 1% precision 5 KΩ linear resistor L with associated electrical components to provide an input signal to one channel of a Honeywell Model 1706 Visicorder. The variable gain of that channel was

set to give full-scale deflection for each piston stroke. Dye from reservoirs R_1 and R_2 runs through Tygon tubing to ports P_1 and P_2 and follows internal holes to opposite sides of the outer orifice rim as depicted in figure 6*b*. Dye from reservoir R_3 is conducted through port P_3 down the hole through the central shaft S and out radial conduits drilled through the centre disk. Since these dye ports are located diametrically opposite their companion ports on plate W, the evolution of vortex ring cores in a meridional plane of the counter-rotating vortex rings may be followed in space and time, but no information about the azimuthal structure can be deduced from this information alone. The heights of each reservoir are individually adjusted prior to a run with the piston fully depressed so that a very small flow rate through the four dye ports is observed, and in this condition the manifold valve regulating the flow is closed. The piston is then slowly raised, drawing water up the chamber, and set to a predetermined height by brass spacers H. After residual fluid motions cease, the manifold valve is reopened and overhead arm A is manually depressed until the piston reaches the bottom of its stroke flush with the opening into chamber K. Attempts were made to obtain a linear displacement of the piston with time, but this was not precisely possible owing to the manual operation of piston movement. The deviation from linear piston displacement is measured by the program factor (Glezer 1988) to be introduced in § 5.

Photographic tracking of the dye blobs marking the vortex ring core sections was obtained with a Pentax ME Super 35 mm camera using Kodak TMZ-3200 black and white film. The camera was mounted some 2 m distant from, and focused on, the central plane of dye motion. The depth of field was sufficient to capture the black rectangular grid G (with 5 cm × 5 cm resolution) inscribed on the vertical wall opposite the camera. Parallax was taken into account by photographing a second grid, temporarily aligned with the central plane, and measuring the deviation between the two grids. Photographs early in a run were acquired using a battery-operated winder at a nominal speed of 2 frames/s, and at later times single-shot photographs were taken manually. Camera firings relative to the piston displacement history were recorded by an electric signal sent to a second channel of the Visicorder. All films were developed in-house and the centres of vortex cores were measured relative to the back-wall grid pattern G from projections of the negatives onto a large screen. Parallax corrections were made to obtain mid-plane trajectory values according to the measured divergence angle of the 135 mm lens. Estimates of the spatial and temporal resolution of the measurements are ± 4 mm and ± 0.02 s, respectively.

The test fluid was normal tap water. Adherence of bubbles to the plastic surfaces after filling the tank with cold tap water obscured viewing and photography. Even more seriously, bubbles attached to the upper surface of horizontal wall W in the neighbourhood of the orifice interfered with the vortex sheet roll-up and formation of the vortex rings. This problem was overcome by filling the tank with very warm water ($T \approx 40$ °C) and allowing the 0.4 m^3 volume to cool to room temperature over a 24 hour period. After wiping all surfaces clean, no subsequent bubble formation was observed. Other impediments to axisymmetric ring formation were tank density stratification due to the ambient vertical temperature gradient in the laboratory and improper alignment of the inner and outer plates forming the orifice. The nearly 1 °C temperature variation of water over the height of the tank was substantially reduced by circulating the water through the system using an external pump with inlet coming from a tube immersed halfway down the tank between B and C and outlet attached to port X on the top of chamber K. Much care was taken in levelling the outer annular plate with respect to the inner disk. Concentricity of the inner disk was maintained by

adjustment of the four adjustable screws mounted at 90° intervals around the baffle disk D positioned near mid-height inside chamber K. The baffle also served to disrupt the motion of the vortex ring pair which forms at the orifice once the piston motion stops. This helped reduce the influence of the upward-propagating vortex ring pair on the downward-propagating ring pair. In spite of these precautions, asymmetric (tilting mode) motion of the inner vortex ring was observed in many runs.

The tilting of the inner vortex rings was finally attributed to the elastic bending of plastic plate W induced while actuating lever L to produce downward piston motion. We have recently learned, however, of new inviscid vortex ring stability calculations (Lough 1993) which go a long way toward providing an explanation for the observed asymmetric motion in our experiment. Lough's results reveal that vortex rings in an unbounded fluid are neutrally stable to tilting-type perturbations, but in the presence of another vortex ring, be it either real or an image ring, this neutral stability is lost owing to the now preferred orientation of the initial disturbance. Although higher modes of instability are also found by Lough, for thin rings the tilting mode is the most unstable over the range of radius ratios encountered in our experiments.

5. Overview of vortex ring pair flow

Assuming axisymmetric formation, the motion of the counter-rotating vortex rings depends on the magnitude of the initial impulse, the time history of the gap-averaged velocity through the orifice, the effective piston stroke, and the diameter ratio of the orifice $\delta = r_i/r_o = d_i/d_o$. The fluid velocity $U_0(t)$ through the gap is readily calculated from the time history of piston displacement scaled by the ratio of orifice area to annular piston area as listed in table 1. Also listed are the orifice areas A, widths W, and radius ratios δ for inner disks 1–5 having diameters d_i. Quantities that characterize $U_0(t)$ determined directly from the strip chart record, are the duration of the impulse T_0, the time-averaged orifice velocity $\bar{U}_0$, the length L of the annular fluid column displaced through the orifice, and the program factor P_f (cf. Glezer 1988) defined as

$$\bar{U}_0 = \frac{1}{T_0}\int_0^{T_0} U_0(t)\,\mathrm{d}t, \tag{5.1}$$

$$L = \bar{U}_0\, T_0, \tag{5.2}$$

$$P_f = \frac{1}{T_0\,\bar{U}_0^2}\int_0^{T_0} U_0(t)^2\,\mathrm{d}t. \tag{5.3}$$

In terms of these quantities the impulse I of liquid forced through the orifice is given by

$$I = \rho A P_f\, \bar{U}_0^2\, T_0. \tag{5.4}$$

The salient non-dimensional parameters governing the motion of the vortex rings are taken to be δ, $I/2\mu A$, $L/2W$, and P_f, where μ is the fluid viscosity. In narrowing the independent parameters to four, we have tacitly assumed that the piston time history curves for each run are similar; in this investigation all piston displacements were nearly linear in time. Actually, the piston histories were composed of generally two, but sometimes three or four sectionally continuous linear segments, and deviation from nominal uniform piston velocity is measured by the program factor defined above. Since the water temperature for each of the experimental runs was in the range 17.5–21.0 °C, the water density was nearly constant at $\rho = 0.9983 \pm 0.0004$ g/cm^3. The

Disk	Run	μ (cP $\times 10^2$)	P_f	$\bar{U}_0$ (cm/s)	$L/2W$	$I/2\mu A$	z'_p/W	ϕ (deg.)	Notes
1	10	1.066	1.073	3.340	0.915	1195	0.928	1.0	1
	11	1.066	1.086	5.228	0.928	1920	0.865	0.2	1
	12	1.067	1.040	2.337	0.932	824	0.975	−4.3	1
	13	1.064	1.051	2.809	0.907	976	0.930	−4.8	1
	14	1.053	1.069	2.633	0.847	878	—	—	1, 3
2	28	0.964	1.039	3.779	1.346	1440	1.60	−2.4	1, 4
	29	0.966	1.053	6.834	1.019	1992	1.57	−1.0	1
	30	0.969	1.012	4.030	0.685	757	—	—	2
	31	0.965	1.021	2.714	1.129	851	2.24	15.8	1
	32	0.966	1.177	3.260	1.013	1056	2.95	6.0	1
	33	0.968	1.187	2.875	1.092	1012	1.57	−1.6	1
	34	0.969	1.061	4.970	0.826	1181	2.60	−3.4	1
3	4	1.022	1.075	4.401	2.667	2370	3.55	−1.9	1
	5	1.022	1.090	5.575	2.741	3126	3.18	−0.6	1
	6	1.075	1.027	2.519	2.424	1119	4.40	−1.1	1
	7	1.070	1.076	4.489	2.556	2215	3.88	2.4	1
	8	1.068	1.089	5.302	2.413	2504	3.74	1.6	1
	9	1.067	1.084	3.735	2.409	1755	3.33	−0.7	1
4	21	0.978	1.128	4.605	2.219	1892	4.55	2.1	1
	22	0.978	1.141	3.968	1.789	1330	—	—	2
	23	0.964	1.135	2.610	1.298	640	—	—	2
	24	0.962	1.077	4.189	1.120	843	—	—	2, 3
	25	0.962	1.110	3.539	1.568	1027	—	—	2, 3
	26	0.964	1.116	2.224	1.110	458	—	—	2
	27	0.966	1.096	3.064	1.981	1105	—	—	1
	35	0.971	1.115	6.952	1.513	1938	4.78	−4.2	1
	36	0.973	1.090	11.587	1.513	3151	4.77	3.3	1
	37	0.976	1.090	4.635	1.513	1257	5.69	−3.2	1
5	15	0.990	1.000	3.780	1.860	906	—	—	2
	16	0.990	1.038	5.852	2.140	1675	—	—	1, 3
	17	0.989	1.044	1.980	2.130	568	—	—	2
	18	0.983	1.295	2.730	2.135	978	8.47	−2.3	1, 5
	19	0.978	1.113	4.192	1.828	1112	—	—	2
	20	0.978	1.163	1.474	0.499	551	—	—	2

TABLE 2. Measured values of viscosity μ, program factor P_f, average orifice fluid velocity $\bar{U}_0$, dimensionless piston stroke $L/2W$, dimensionless fluid impulse $I/2\mu A$, dimensionless inner ring penetration distance z'_p/W, and estimated tilt angle ϕ of the inner vortex ring at maximum penetration. Notes: 1, inner ring returned; 2, inner ring did not return; 3, no photographic record; 4, no synchronized time record for camera firings; 5, inner ring became turbulent near the top of its trajectory.

fluid viscosity, however, varied slightly from run to run, and its value along with other pertinent measurements are listed in table 2. The 34 experimental runs in this table are categorized according to inner disk number (cf. table 1).

The parameter space of all reported experiments is plotted in figure 7. Here $L/(d_o - d_i) = L/2W$ is the non-dimensional length of fluid displaced through the orifice and $I/2\mu A$ is the dimensionless impulse. All counter-rotating vortex rings were observed to be laminar on formation and, with the exception of run 18, throughout their entire trajectories. For a given piston program, Glezer (1988) has shown that vortex rings produced through the open end of a circular tube will be laminar or turbulent on formation depending on the non-dimensional piston displacement L/d_o and the Reynolds number γ_o/ν, or equivalently, the dimensionless impulse $I/2\mu A$. His

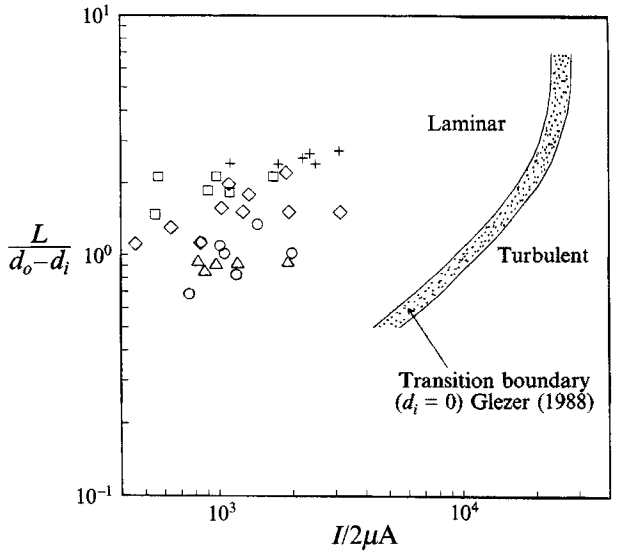

FIGURE 7. Parameter space for experiments conducted; L is the slug length of fluid displaced through the orifice and I is the total impulse. △, $\delta = 0.595$; ○, $\delta = 0.726$; +, $\delta = 0.800$; ◇, $\delta = 0.833$; □, $\delta = 0.867$.

measured transition boundary separating laminar from turbulent vortex rings on formation is plotted in figure 7 for comparison with the present laminar counter-rotating vortex ring data.

Although the primary goal of the experiment was to determine the trajectories of laminar counter-rotating vortex rings, other interesting features of ring-pair motion soon became apparent. In the following sections we present observations of the vortex ring formation process, flow asymmetry, individual vortex ring instability, and interacting ring pair instability.

5.1. *Vortex ring formation process*

Careful observations of piston-generated vortex rings through a circular tube have been reported by Didden (1979). In his experiment the piston was programmed to achieve constant velocity throughout, with the exception of an initial acceleration lasting 10% of the period of piston movement. He reported that the evolution to a constant-diameter vortex ring downstream of the tube takes place in two stages. In the first stage, the vortical fluid rolls up into a toroidal spiral whose major diameter increases with downstream distance. For these laminarly produced vortex ring pairs, the spiral centre generated at fixed δ follows common (self-similar) trajectories independent of the orifice Reynolds number, but with forward penetration depending on the piston stroke. In the second stage after termination of piston motion, the vortex ring propagates freely away from the open end and simultaneously induces the formation of a secondary counter-rotating vortex ring with axis in the exit plane of the tube. The initial forward trajectory of the free vortex ring is accompanied by a sudden decrease in ring diameter owing mainly to the influence of the nozzle wall. In earlier work Didden (1977) showed, and Leiss (1978) subsequently confirmed, that the vortex trajectory is independent of orifice Reynolds number up to $Re_o = 10^4$.

All of the features reported by Didden (1979) for single vortex ring formation have been observed in vortex ring pair formation. Figure 8 shows the averaged near-orifice

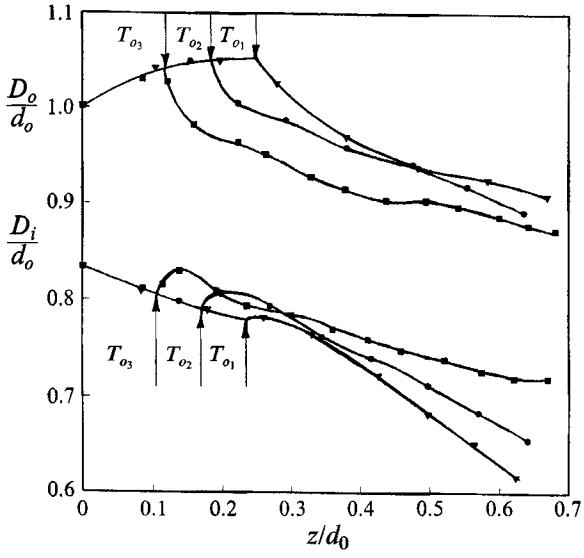

FIGURE 8. Near-orifice trajectories for runs 21, 22, 23 showing the self-similar nature of vortex ring formation. Following Didden (1979) we have plotted the instantaneous ring diameters D_o and D_i normalized by the outer orifice diameter d_o. The respective dimensionless fluid slug lengths are: ▼ $L/2W = 2.22$, ● $L/2W = 1.79$, ■ $L/2W = 1.30$. The respective piston stroke durations are respectively $T_{0_1} = 1.55$ s, $T_{0_2} = 1.45$ s and $T_{0_3} = 1.60$ s.

trajectories of vortex rings for runs 21, 22 and 23 which were generated with nearly identical program factors $P_f = 1.135 \pm 0.0007$, but with decreasing effective piston strokes $L = 7.14$ cm, 5.76 cm, and 4.18 cm, respectively. The corresponding periods of piston movement for these runs are $T_{0_1} = 1.55$ s, $T_{0_2} = 1.45$ s, and $T_{0_3} = 1.60$ s. The distances travelled by the inner and outer vortex rings during these periods are indicated by the arrows in figure 8. Even with the paucity of data in the formation region, common trajectories of the developing spiral cores can be discerned. Faired curves drawn through the data away from the roll-up trajectories mark the paths of free ring motion. At the end of the piston stroke, a secondary vortex ring pair, opposite in sense to the primary ring pair, forms at the edge of the annular orifice and propagates vertically back up chamber K until it impinges on baffle plate B, spreads radially, and dissipates. If one neglects the effect of this secondary ring pair, an analysis of the motion of the primary ring pair taking into account its image behind a solid wall unequivocally shows that both the inner and outer vortex rings must decrease in diameter as they move away from the wall. This in fact is observed for all rings at distances $z/d_o > 0.3$, but the initial free motion of the ring pair is appreciably affected by the presence of the orifice and the secondary ring pair when $z/d_o < 0.3$. The effect of the secondary ring pair is to draw the primary ring pair back towards the orifice, and this results in an initial increase in diameter of the inner ring and a more rapid decrease in diameter of the outer ring. The orifice Reynolds numbers for runs 21, 22, and 23 are $Re_o = 2W\bar{U}_0/\nu = 1515$, 1306 and 869, respectively.

Very recently, a direct numerical simulation of the inviscid spiral roll-up process in Didden's (1979) experiment has been reported by Nitsche (1992). She has accurately reproduced the formation, growth and trajectory of the primary vortex ring and also the formation and growth of the secondary vortex ring inside the nozzle. The common trajectories of spiral vortex ring roll-up is confirmed and the evolution of the spiral into an elliptical form at later times is observed both in the inviscid computation and in

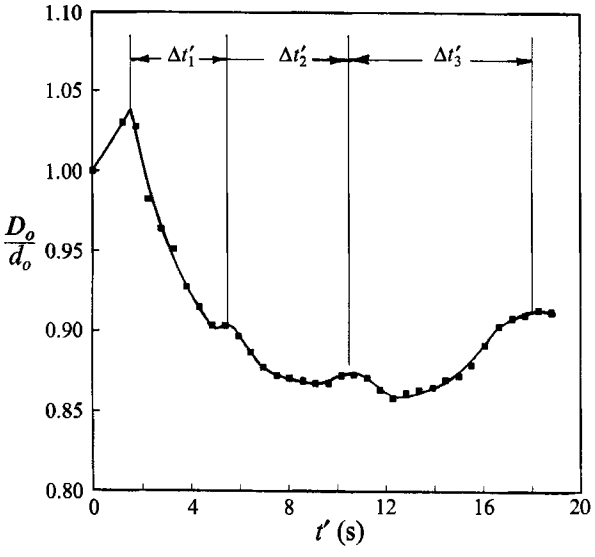

FIGURE 9. Average outer vortex ring diameter D_o normalized by outer orifice diameter d_o as a function of time for run 23. The first three undulation periods of the vortex core are $\Delta t_1' = 3.95$ s, $\Delta t_2' = 5.00$ s and $\Delta t_3' = 7.5$ s.

Didden's viscous experiment. In carrying out the computation to larger times, Nitsche observed an oscillation of the ring diameter with slightly increasing oscillation period $\Delta t'$, which was interpreted as a 'tumbling' of the elliptical vortex core. A similar oscillation of outer ring diameter is observed in the present experiments. Figure 9 shows the average trajectory of the outer vortex ring corresponding to run 23. In the second stage of motion, three oscillations of increasing period $\Delta t_3' > \Delta t_2' > \Delta t_1'$ superimposed on the radially shrinking ring trajectory are discerned. The ratio of the first two periods in Nitsche's simulation is $\Delta t_2'/\Delta t_1' = 1.13$ and the ratios observed here are $\Delta t_2'/\Delta t_1' = 1.26$ and $\Delta t_3/\Delta t_2 = 1.50$. We do not know if the outer vortex ring core was pulsating or rotating. However, this qualitative correspondence between our measurements and the calculations of Nitsche (1992), both in the self-similar nature of axisymmetric vortex sheet roll-up and in the vortex ring oscillation suggest that the vortex dynamics at early times in the present experiment are basically an inviscid phenomenon.

5.2. *Vortex ring stability*

Observations of azimuthal instabilities on vortex rings date back at least to Thompson & Newall (1885). Krutzsch (1939) found that instability waves may be non-uniformly distributed around the ring and that subsequent breakdown on the vortex ring may be initiated locally (Saffman 1978). Many experimental and analytical investigations on the stability of laminarly formed vortex rings have appeared recently, notably those by Maxworthy (1974, 1977), Widnall, Bliss & Tsai (1974), Liess & Didden (1976) and Saffman (1978). Saffman (1978) used information from the experiments of Liess & Didden (1976) to choose various constants for his theory predicting the number N of azimuthal waves appearing on a single vortex ring at instability. Good agreement between the theory and independent measurements of Maxworthy (1977) for N was found up to the highest experimental Reynolds number available for comparison, $Re_o = \bar{U}_0 d_o/\nu = 8 \times 10^4$, except in the region $3 \times 10^4 < Re_o < 5 \times 10^4$ where Maxworthy observed a 'bimodal instability'.

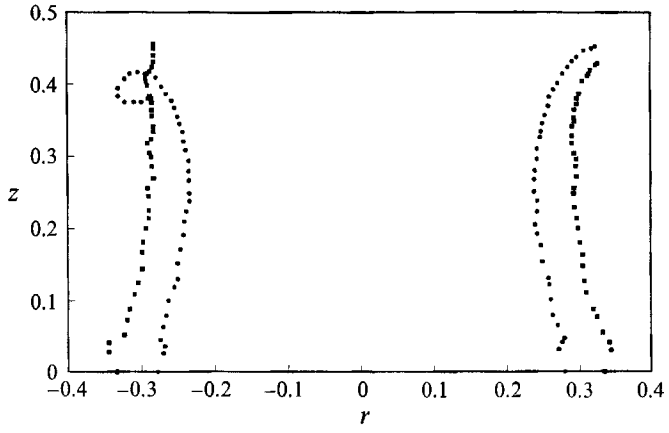

FIGURE 10. Vortex ring pair trajectory for run 23 at $\delta = 0.833$ showing mutual instability leading to disintegration of the organized motion.

Assuming that the orifice Reynolds number $Re_o = \bar{U}_0(d_o - d_i)/\nu$ for our vortex ring pair may be used in Saffman's theory, one finds $2 < N < 7$ waves on the outer vortex ring for the range of orifice Reynolds numbers $520 < Re_o < 3480$ covered in the present experiments. Dye injection at opposite sides of the annulus can provide some information on ring–ring interactions, but reveals nothing about possible azimuthal instabilities riding on each individual ring. Complete visualization around the vortex rings was made possible by gently injecting dye over the upper surface of the inner and outer orifice plates accessed via port X on the top of chamber K (cf. figure 6*b*). A few runs using disk 2 with radius ratio $\delta = 0.726$ at $Re \approx 1800$ revealed four and sometimes five waves around the outer vortex ring, with no waves apparent on the inner ring, apart from the irrepressible mode-one tilt. At this Reynolds number, the results provided in figure 3 of Saffman (1978), strictly valid for a single vortex ring, give $N = 5$, but very close to transition to $N = 6$. In the visualization, the waves appeared uniformly distributed around the outer ring and grew to a fixed (or slowly varying) amplitude of about two core diameters. The vortex ring continued to propagate with its 'frozen' corrugation pattern down to the bottom of the tank where, there being sufficient dye remaining for visualization, its collision with the lower boundary could be observed. During the collision process the ring rebounded off the bottom wall once, and sometimes twice, in a fashion similar to the numerical simulation given in figure 5(*a*).

In experiments using disks 4 and 5 which provide the narrowest gaps tested, the vortex ring pairs often travelled forward in close proximity for many gap widths W. The motion generally ended in an abrupt ring–ring instability, wherein the inner ring wrapped rapidly around the outer, at least in certain azimuthal sections. This process is evident in figure 10 which shows the ring pair trajectory for run 23 corresponding to $\delta = 0.833$ with dimensionless impulse $I/2\mu A = 640$. A section of the inner ring filament is observed to wrap around the stronger outer ring on the left, while on the right the ring filaments veered off together. At this point the dye in the vortex cores usually diffused to an extent that further identification of the individual rings was not possible. The asymmetry in this ring–ring instability exhibits features similar to the ring–ring interaction simulated in the numerical experiments of Swearingen *et al.* (1992) for normal incident collision of a vortex ring with a wall as described in the introduction. In the six experiments using disk 5 for which $\delta = 0.867$, the rings propagated together

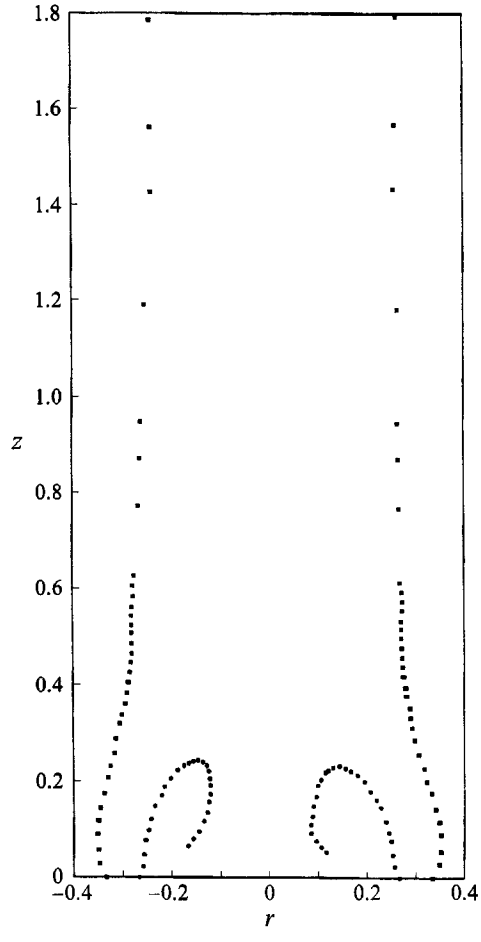

FIGURE 11. Vortex ring pair trajectory for run 4 at $\delta = 0.800$ showing return of the inner vortex ring.

in the manner described above with the exception of run 23. In that case the spiral coils in the core of the inner ring burst into a turbulent patch just before reaching maximum penetration. The inner ring then continued its motion with no apparent interruption, contracting in diameter over the top of its trajectory, and propagated in a very symmetric manner backward to eventually collide with the inner orifice disk. The trajectory for this run plotted in figure 17(*b*) is introduced in §6.

5.3. *Flow symmetry*

By now it is understood from the experiments that the rings comprising a ring pair either propagate together until diffusive effects or vortex ring instability destroys the coherent motion, or the inner ring advances to some maximum axial position, reverses its direction and returns to the orifice wall, leaving the outer ring to continue its forward motion unabated. An example of the latter case is provided by run 4 with trajectories plotted in figure 11. Note that although both halves of the inner ring penetrate equally far from the orifice wall, there is an obvious asymmetry in their motion. For example, the inner core on the right moves radially inward to $r'/a \approx 0.08$ while the inner core on the left goes no further than $r'/a \approx 0.115$. This skewed leftward

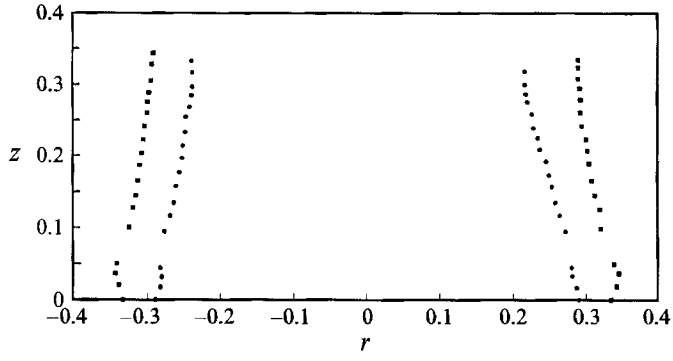

FIGURE 12. Vortex ring pair trajectory for run 15 at $\delta = 0.867$ showing balanced ring pair propagation before ultimate decay.

movement of the inner ring is observed to impart a very slight rightward impulse to the outer ring, an evident consequence of conservation of zero total radial momentum for the system. As a measure of asymmetry, we have recorded the angle of tilt ϕ of the inner vortex ring at the top of its trajectory in the plane of visualization. For run 4 the angle is $\phi = -1.9°$, and tilt angles for all other inner rings which reversed their direction of motion are given in table 2. Note that the rings have equal probability of tilting to the left or right and, with two exceptions in the measured data, $|\phi| \leqslant 5°$.

Run 15 provides an example of counter-rotating vortex rings that propagate together as a coherent unit. The trajectory for this ring pair plotted in figure 12 shows the weaker inner ring always lagging slightly behind the stronger outer ring. In this position the balance between ring–ring induction and diffusion can be maintained (cf. figure 5*a*). It has been observed in other runs that whenever the inner ring moves abreast of the outer ring, the former is induced to move rapidly forward and around the latter, and the coherent motion is inevitably destroyed by ring–ring instability. In one or two instances, however, it appeared that the weaker inner ring actually merged with the outer ring without visible instability.

5.4. *Inner ring penetration*

As mentioned in the introduction, Kambe & Takao (1971) reported, *inter alia*, qualitative results of a single experiment in air designed to initiate counter-rotating vortex rings through an annular orifice by impulsive piston motion, much like in the present investigation. Three cine frames of a motion picture given in their figure 11, interpreted by a schematical illustration in their figure 10, shows the formation of the ring pair and the immediate reversal of the inner ring in the second stage of free vortex motion. The orifice radius ratio for their experiment, the impulse imparted to the fluid by a sudden hit to the end of the piston rod, and the dimensional penetration distance z'_p of the inner ring at its reversal point, were not reported. The values of these parameters for the single experiment reported by Kambe & Takao (1971) are estimated in the Appendix to be $\delta = 0.6$, $I/2\mu A = 7500 \pm 500$, and $0.5 < z'_p/W < 1.0$.

As may be seen from the results in table 2, the inner ring reversed its direction in 24 of the 34 experimental runs. In figure 13 we plot the normalized inner ring penetration distance z'_p/W as a function of the dimensionless impulse $I/2\mu A$ for the 19 most symmetrical runs satisfying $|\phi| < 5°$. The distance z'_p is taken to be the maximum average axial position of the left and right dyed cores. Each data set in this figure corresponds to a different radius ratio δ and is, for lack of more precise data, fitted with

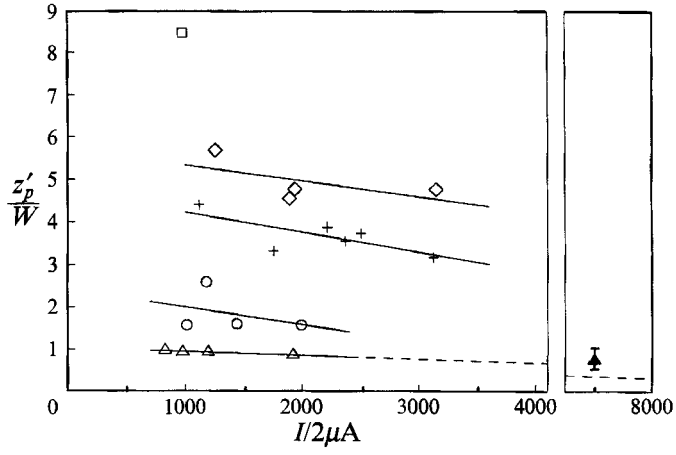

FIGURE 13. Normalized penetration distance of the inner vortex ring as a function of non-dimensional impulse with δ as a parameter with symbols as in figure 7. These results exclude all rings having tilt angles ϕ exceeding 5° at maximum penetration (cf. table 2). The solid lines are least-squares linear fits to the each data set and the dashed line is a linear extrapolation for $\delta = 0.595$.

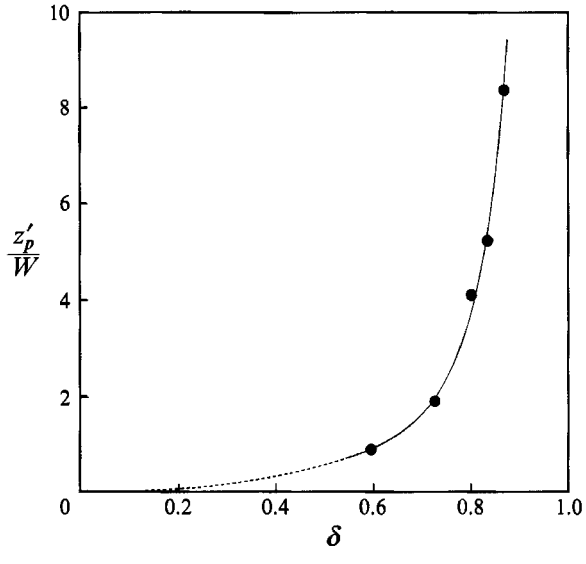

FIGURE 14. Penetration distance of the inner vortex ring at $I/2\mu A = 978$ obtained from the fitted curves in figure 13. The solid curve is the power law fit to $(1-\eta)$ given by equation (5.5) in the text, while the dashed curve is the unique cubic fit through the origin matching slope and value to equation (5.5) at $\delta = 0.55$.

a least-squares linear curve fit. The estimated data point for $\delta = 0.6$ in the experiment of Kambe & Takao (1971) should correspond to the trend of data measured here for $\delta = 0.595$. Indeed, the dashed line in figure 13 corresponding to an extrapolation of the linear fit is seen to fit as well as might be expected with the estimated experimental point of Kambe & Takao (1971) determined in the Appendix. In fact, the extrapolation cannot follow a straight line, but is expected to approach $z'_p/W = 0$ from above asymptotically as $I/2\mu A \to \infty$.

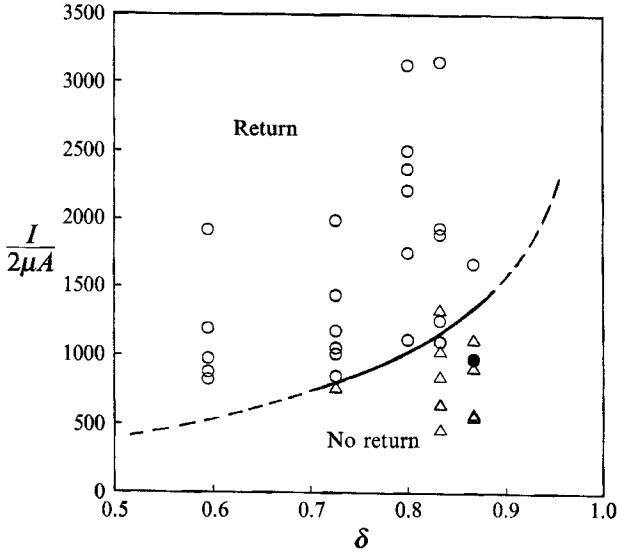

FIGURE 15. Regime diagram for return of the inner vortex ring: ○, rings that returned; △, rings that did not return; ●, ring that went turbulent at the top of its trajectory. The demarcation separating rings which returned from those that did not is drawn assuming results to be independent of the piston stroke.

The effect of radius ratio on inner ring penetration distance can be determined at the common value $I/2\mu A = 978$ corresponding to the single data point for $\delta = 0.867$ in figure 13 using the curve fits to the remaining four values of δ. The results plotted in figure 14 exhibit a faster-than-exponential rise in normalized penetration with radius ratio δ. In fact, a very good approximation to the data in the range $0.595 \leqslant \delta \leqslant 0.867$ is given by the least-squares polynomial fit

$$\frac{z_p'}{W} = \frac{0.156}{(1-\delta)^{1.99}}. \tag{5.5}$$

The dashed curve is the cubic fit through the origin matching slope and value to (5.5) at $\delta = 0.55$. The trend of (5.5) is consistent with $z_p'/W \to \infty$ as $\delta \to 1$ for parallel rectilinear vortex rings.

The experimentally determined boundary separating inner rings that return from those that do not in impulse–radius ratio space is given by the solid curve in figure 15, valid for $0.595 < \delta < 0.867$. In this figure all circles indicate rings that returned, and triangles correspond to rings that did not return. The solid circle is the data point corresponding to run 18 for which the inner ring apparently underwent transition to turbulence near the top of its trajectory. In presenting this figure we have tacitly assumed that the return boundary is independent of piston stroke L. This is not expected to be correct since it may be inferred from the studies by Liess & Didden (1976) and Didden (1979) that vortex ring motions generated by the same impulse but with different piston strokes will have measurably different trajectories. However, the data presented here over the limited range of $L/2W$ exhibit some consistency, and the solid line gives the best estimate of the demarcation boundary. The dashed curves to lower and higher values of δ represent expected trends in those directions, viz. $I/2\mu A \to 0$ as $\delta \to 0$, and $I/2\mu A \to \infty$ as $\delta \to 1$. We note that our estimated data point

$I/2\mu A \approx 7500$, $\delta = 0.6$ for the returned inner ring observed by Kambe & Takao (1971) is consistent with the results in figure 15.

6. Comparison with numerical simulation

In this section we make a comparison between three of our experimental runs with numerical simulations of these as presented in §3. Recall that our simulation does not model the formation process of the vortex rings. It assumes they exist at a prescribed position in a closed cylindrical container at some initial time t_0 with a structure based upon the viscous rectilinear vortex solution. In the formation process the outer and inner rings tend to expand and contract respectively, in the radial direction, as long as the piston is forcing fluid through the annular gap. This process ceases, and can be seen to cease, in the plots of the experimental trajectories in figure 8, when the piston is brought to rest. Only after that time is it appropriate to make a comparison between the present viscous calculations and experiment.

As we have seen in earlier sections, our experiments yield the time history of the vortex-ring trajectories, with the time history of the driving piston itself. What we are not able to infer directly is the initial circulation about each vortex ring, and hence the Reynolds number $Re = \gamma_o/\nu$ of the flow. An estimate of the circulation may be made as follows. Consider a two-dimensional slit through which fluid is forced, to form a rectilinear vortex pair. Suppose that the fluid emerges from the slit $|z| < 1$ as a slug flow with axial velocity $w = w_0$ for $|z| < 1$ and $w = 0$ for $|z| > 1$, where w_0 is a constant. The circulation $\delta\gamma$ which is shed from one edge of the slit, say $z = 1$, in a time δt is, by Stokes's theorem,

$$\delta\gamma = \int_A \zeta \, \mathrm{d}A = -\delta t \int_0^{z_1} w \frac{\partial w}{\partial z} \mathrm{d}z = -\delta t \int_{w_0}^{0} w \, \mathrm{d}w, \tag{6.1}$$

from which we infer that $\mathrm{d}\gamma/\mathrm{d}t = \frac{1}{2}w_0^2$. If the time history of the piston which drives such a motion is known, then $w_0(t)$ can be inferred, and the total circulation shed calculated by simple quadrature. Of course, this is a two-dimensional argument, and if it is applied to our annular slit aperature does not distinguish between the inner and outer vortex rings, which we may expect to differ in strength. Pullin (1979) has argued that with all other parameters held fixed, the circulation about a vortex ring may be expected to vary as the four-thirds power of its radius. From this argument we may infer that the inner ring, of the pair shed from the annular orifice, is weaker than the outer.

Whilst the above arguments give reasonable order of magnitude estimates for the circulation about each vortex ring, we have found that they consistently underestimate the circulation about the outer ring, and overestimate that about the inner. (By way of comparison, we note that Didden (1979) measured circulation strengths for a single vortex ring in excess of that given by a simple slug flow model. Extensive discussions on this point are given by Didden (1982) and Maxworthy (1977)). As a consequence we have proceeded, in the following pragmatic manner, to determine the circulations. The circulation about the outer ring γ_o, and hence the Reynolds number Re, is chosen to give the correct timescale when compared with the experiments. By that we mean that γ_o is chosen in such a manner as to ensure that in a given interval of time the outer vortex ring propagates the same axial distance as the observed outer ring. The inner ring circulation is then chosen to ensure that the calculated maximum penetration distance of the inner vortex ring coincides with the observed maximum penetration distance.

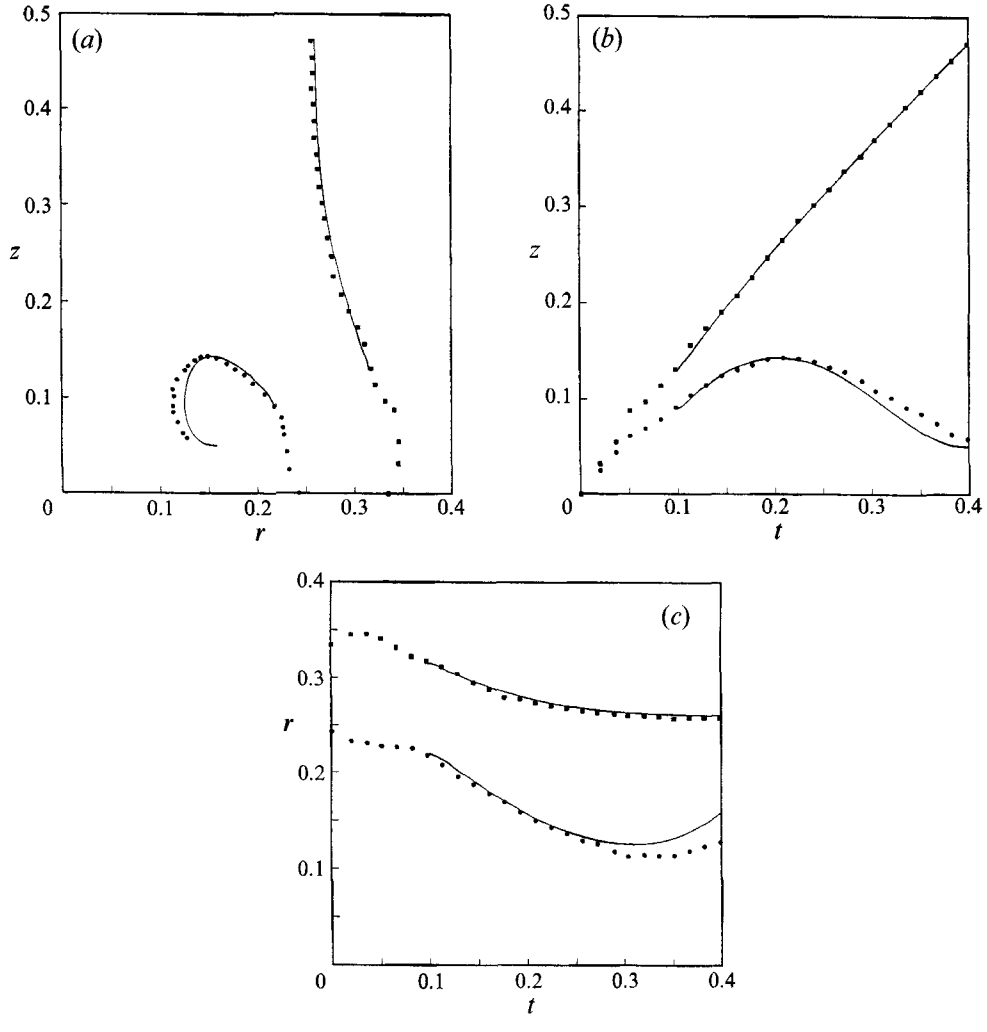

FIGURE 16. A comparison between averaged measurements (●, ■) for run 33 and the calculated (—) values of (*a*) vortex ring trajectories, and the time evolution of (*b*) the axial and (*c*) the radial positions of the inner and outer rings; $\delta = 0.726$, $Re = 2100$, $\gamma_i/\gamma_o = -0.70$ and $t_0 = 0.1$.

In figures 16–17 we show a comparison between simulation and experiment for runs 33, 5, and 18 corresponding to three of the annular gaps available to us. In these figures we have averaged the radial and axial position measurements obtained at opposite sides of the vortex rings in an attempt to find the best axisymmetric representation for ring core trajectories. Figure 16(*a*) presents the measured trajectories for experimental conditions $I/2\mu A = 1012$ and $\delta = 0.726$ for which we have chosen $Re = 2100$ and $\gamma_i/\gamma_o = -0.70$ for numerical calculations started at the dimensionless time $t_0 = 0.1$. The time evolution up to $t = 0.4$ of the axial and radial position of each vortex for this run is presented in figures 16(*b*) and 16(*c*), respectively. Figure 17(*a*) shows the average trajectories for $\delta = 0.8$ with $I/2\mu A = 3126$ and figure 17(*b*) gives trajectories for the narrowest gap $\delta = 0.867$ at $I/2\mu A = 1112$. We consider the agreement between experiment and calculation to be good considering that the magnitudes of the initial circulations are not known.

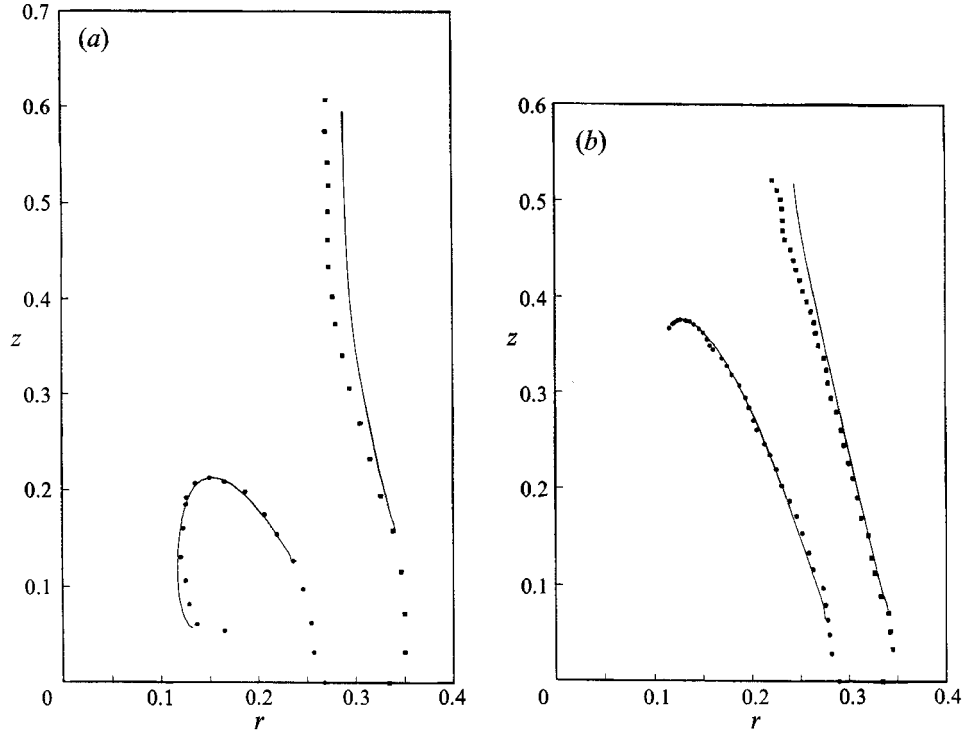

FIGURE 17. (*a*) As in figure 16(*a*) but for run 5; $\delta = 0.800$, $Re = 4431$, $\gamma_i/\gamma_o = -0.600$ and $t_0 = 0.125$. (*b*) As in figure 16(*a*) but for run 18; $\delta = 0.867$, $Re = 1336$, $\gamma_i/\gamma_o = -0.819$ and $t_0 = 0.037$.

7. Discussion and conclusion

A major conclusion of the numerical simulation is the prediction of the existence, at least in a quasi-steady sense, of vortex ring pairs. For inviscid flow a calculation based upon thin rings, the result of which is equation (3.1), is unequivocal in its prediction of such a configuration. For a viscous fluid, in which there is a continuous redistribution of vorticity by diffusion, a steady flow is not possible. Nevertheless our numerical simulations predict that the concept of a vortex ring pair is a valid one in a quasi-steady sense.

We have conducted experiments on the formation and movement of counter-rotating vortex rings generated by fluid displacement through annular orifices over the range of radius ratios $0.595 < \delta < 0.867$, dimensionless piston displacements $0.7 < L/2W < 2.7$ and dimensionless impulses $550 < I/2\mu A < 3150$. All vortices were laminar on formation in agreement with the laminar–turbulent transition boundary measured by Gleezer (1978). Piston velocities deviated marginally from their average constant value $\bar{U}_0$, and the program factor measuring deviations had an average value $P_f = 1.09$. According to the analysis by Saffman (1978), the laminar outer vortex ring should have always undergone azimuthal instability of the type observed by Krutzsch (1939), Maxworthy (1972) and others, with modal wavenumbers in the range $2 < N < 7$, if the annular orifice Reynolds number $Re_o = \bar{U}_0(d_o - d_i)/\nu$ may be substituted for the circular orifice Reynolds number $Re_o = \bar{U}_0 d_o/\nu$ used in Saffman's analysis. Visualization experiments for $\delta = 0.726$ showed that the instability amplitude grew slowly to about two viscous core diameters and remained in an approximately frozen pattern on the ring during its trajectory to the bottom of the tank. Measurements

at the largest radius ratios exhibited more active involvement of the outer ring in its interaction with the weaker counter-rotating inner ring during the final stages of vortex ring pair breakdown.

The axisymmetric roll-up of the inner and outer vortex sheets is observed to follow common trajectories independent of the orifice Reynolds number, dependent only on the orifice radius ratio. This compares favourably with observations by Didden (1979) for isolated vortex rings generated through the end of a circular tube. An oscillation of the outer (and, perceptibly, sometimes the inner) vortex ring has been observed. Nitsche (1992), in an inviscid simulation of Didden's (1979) experiments carried out to large times, found a similar ring diameter oscillation attributed to a tumbling of the elliptical vortex core. In both cases the average oscillation period decreases with each subsequent oscillation.

Reversal of the direction of propagation of the inner vortex ring depends primarily on δ and $I/2\mu A$ for the restricted range of piston strokes used in the present experiment according to the results in figure 15. The demarcation between rings that return and those that do not evidently follows a monotone curve increasing from low values of δ and $I/2\mu A$ and tending toward the asymptotic limit $I/2\mu A \to \infty$ as $\delta \to 1$, corresponding to rectilinear vortex pairs. Furthermore, the penetration distances measured in this experiment are in qualitatively good agreement with the estimated data point for the single experiment reported by Kambe & Takao (1971).

The comparison of calculated trajectories of the vortex rings in both time and space with the measured trajectories, made by judicious choice of the initial circulation strengths of the vortex rings at an initial position in their second stage of free vortex motion, is considered good. And we remark that in the absence of any sophisticated experimental technique to measure the circulation about each ring, the numerical simulation itself provides a tool to determine these circulations. Of interest would be the calculation of the viscous second stage of vortex trajectories from knowledge of their initial positions and circulation strengths at the end of an inviscid vortex sheet roll-up calculation such as that given by Nitsche (1992). Indeed, for the Reynolds numbers covered in the present investigation, it appears that the motion of vortex ring pairs is, for the most part, governed by inviscid dynamics. Hence, a complete inviscid calculation of the entire vortex ring pair motion would be equally interesting.

P.W.D. gives his sincere appreciation to SERC for a Visiting Fellowship to carry out this research at the University of East Anglia while on sabbatical leave from the University of Colorado. Machinists Keith Randell and Chris Hindle did an excellent job in construction of the experimental facility and offered valuable suggestions in the design of the apparatus. We thank Professor John Davies of the School of Physics for providing bench space for the experimental apparatus and Kadir Kirkkopru for help with some parts of the experiment. Members of School of Mathematics contributed to stimulating discussions and otherwise made for a memorable sabbatical leave for P.D.W., particularly Dave Needham and Nigel Scott.

Appendix

The purpose of the appendix is to outline our procedure for estimating the non-dimensional parameters δ and $I/2\mu A$ for the generation of a counter-rotating vortex ring pair by impulsive displacement of air through an annular orifice in the experiment of Kambe & Takao (1971). From their statement that all variously shaped orifices were made to have areas equal to that of a circular orifice of diameter 6 cm, and assuming

as shown in their figure 7(*a*) that the mean orifice diameter was equal to the circular orifice diameter, one finds $\delta = 0.6$ for their set-up. The inner ring penetration distance z'_p, cannot be determined precisely, but from the illustration in their figure 10 it is readily inferred that $0.5 < z'_p/W < 1.0$.

The basic assumption entertained here is that the impulse imparted to the air through the annular orifice in the experiments of Kambe & Takao (1971) was comparable to the impulse imparted to air through the circular orifice for which quantitative information was given. We begin with the asymptotic formula for inviscid motion at velocity U of a circular vortex ring of diameter D with uniform vorticity core of diameter d possessing circulation Γ (Lamb 1932)

$$U = \frac{\Gamma}{2\pi D}\left(\ln\left(\frac{8D}{d}\right) - \frac{1}{4}\right) \tag{A 1}$$

valid for small core diameters $d \ll D$. As shown by Glezer (1988), the impulse imparted to a vortex ring is given by

$$\frac{I}{2\mu A} = \frac{\Gamma}{\nu} \tag{A 2}$$

and use of (A 1) yields

$$\frac{I}{2\mu A} = \frac{2\pi UD}{\nu}\left[\ln\left(\frac{8D}{d}\right) - \frac{1}{4}\right]^{-1}. \tag{A 3}$$

This represents the non-dimensional impulse generated through a circular orifice of area $A = \frac{1}{4}\pi(d_o)^2$. Using Kambe & Takao's measured values $U = 150$ cm/s, $D \approx 6$ cm, and $\nu = 0.15$ cm^2/s for a vortex ring produced through a circular orifice, (A 3) gives

$$\frac{I}{2\mu A} = 37\,700\left[\ln\left(\frac{8D}{d}\right) - \frac{1}{4}\right]^{-1}. \tag{A 4}$$

The ratio d/D is not known, but is expected to fall in the range $0.01 < d/D < 0.1$ for typical vortex ring experiments in air. Using (A 4) one finds $I/2\mu A = 7260$, 7430, and 8610 for respective values $d/D = 0.01$, 0.05 and 0.1. As a representative value we take $I/2\mu A = 7500$ as the impulse imparted to a circular ring in their experiments. According to our premise that the fluid impulse through the annular orifice was comparable to the fluid impulse through the circular orifice, our estimates for the non-dimensional parameters in the counter-rotating vortex ring experiment of Kambe & Takao (1971) are $\delta = 0.6$ and $I/2\mu A = 7500$.

REFERENCES

Acheson, D. J. 1990 *Elementary Fluid Dynamics.* Oxford University Press.

Cerra, A. W. & Smith, C. R. 1983 Experimental observations of vortex ring interaction with the fluid adjacent to a surface. *Rep.* RM-4. Department of Mechanical Engineering and Mechanics, Lehigh University, Bethlehem, PA.

Didden, N. 1977 Untersuchung laminarer, instabiler Ringwirbel mittels Laser-Doppler-Anemometrie. Mitt. aus dem MPI fur Stromungsforschung und der AVA Nr. 64, Gottingen.

Didden, N. 1979 On the formation of vortex rings: Rolling-up and production of circulation. *Z. Angew. Math. Phys.* **30**, 101–116.

Didden, N. 1982 On vortex formation and interaction with solid boundaries. In *Vortex Motion* (ed. E.-A. Muller), pp. 1–17, Vieweg.

Dommermuth, D. G. & Yue, D. K. P. 1990 A numerical study of three-dimensional viscous interactions of vortices with a free surface. *Proc. 18th Symp. on Naval Hydrodynamics, August*

19–24, 1990, The University of Michigan, Ann Arbor, pp. 727–788. Washington: National Academy of Sciences.

GLEZER, A. 1988 The formation of vortex rings. *Phys. Fluids* **31**, 3532–3542.

KAMBE, T. & TAKAO, T. 1971 Motion of distorted vortex rings. *J. Phys. Soc. Japan* **31**, 591–599.

KRUTZSCH, C.-H. 1939 Uber eine experimentell beobachtete Erscheinung an Wirbelringen bei ihrer translatorischen Bewegung in wirklichen Flussigkeiten, *Ann. Phys.* **5**, Band (35), 497–523.

LAMB, H. 1932 *Hydrodynamics*. Dover.

LASHERAS, J. C., LECUONA, A. & RODRIGUEZ, P. 1991 Three-dimensional vorticity dynamics in the near field of co-flowing forced jets. *AMS-SIAM Summer Seminar on Vortex Dynamics and Vortex Methods* (ed. C. Anderson & C. Greengard). American Mathematical Society series in Lectures in Applied Mathematics.

LIESS, C. 1978 Experimentelle Untersuchung des Lebenslaufs von Ringwirbeln. *Rep.* 1/1978. MPI fur Stromungsforschung Gottingen.

LIESS, C. & DIDDEN, N. 1976 Experimente zum Einfluss der Anfangsbedingungen auf die Instabilitat von Ringwirbeln. *Z. Angew. Math. Mech.* **56**, 206–208.

LOUGH, M. 1993 On the motion of thin core vortex filaments: the equations of motion and their application to specific problems. PhD thesis, California Institute of Technology (in preparation).

MARGARVEY, R. H. & MACLATCHY, C. S. 1984 The disintegration of vortex rings. *Canadian J. Phys.* **42**, 684–689.

MAXWORTHY, T. 1974 Turbulent vortex rings. *J. Fluid Mech.* **64**, 227–239.

MAXWORTHY, T. 1977 Some experimental studies of vortex rings. *J. Fluid Mech.* **81**, 465–495.

NITSCHE, M. 1992 Axisymmetric vortex sheet roll-up. PhD Thesis, Department of Mathematics, The University of Michigan.

ORLANDI, P. 1990 Vortex dipole rebound from a wall. *Phys Fluids* A **2**, 1429–1436.

PULLIN, D. I. 1979 Vortex ring formation at tube and orifice openings. *Phys. Fluids* **22**, 401–403.

SAFFMAN, P. G. 1978 The number of waves on unstable vortex rings. *J. Fluid Mech.* **84**, 625–639.

SHARIFF, K. & LEONARD, A. 1992 Vortex rings. *Ann. Rev. Fluid Mech.* **24**, 235–279.

SWEARINGEN, J. D., CROUCH, J. D. & HANDLER, R. A. 1993 Dynamics and stability of a vortex ring impacting on a solid boundary. *J. Fluid Mech.* (to be submitted).

THOMSON, J. J. & NEWALL, M. A. 1885 On the formation of vortex rings by drops falling into liquids, and some allied phenomena. *Proc. R. Soc. Lond.* A **39**, 416–436.

VAN DYKE, M. D. 1982 *An Album of Fluid Motion*. Parabolic.

WIDNALL, S. E., BLISS, D. B. & TSAI, C.-Y. 1974 The instability of short waves on a vortex ring. *J. Fluid Mech.* **66**, 35–47.

WOODS, L. C. 1954 A note on the numerical solution of fourth-order differential equations. *Aero. Q.* **5**, 176–182.

YAMADA, H. & MATSUI, T. 1978 Preliminary study of mutual slip-through of a pair of vortices. *Phys. Fluids* **21**, 292–294.

YAMADA, H. & MATSUI, T. 1982 Visualization of vortex interaction using smoke-wire technique. In *Flow Visualization II* (ed. W. Merzkirch), pp. 355–359. Hemisphere.